RESEARCH ARTICLE

Check for updates

Selective syntheses of homoleptic Ir(III) complexes bearing di-CF₃-functionalized benzoimidazol-2-ylidenes for generation of blue phosphorescence†

Jie Yan, [ID] ‡[a] Yi Pan, [ID] ‡[a] I-Che Peng,‡[b] Wen-Yi Hung, [ID] *[b] Bingjie Hu,[a] Guowei Ni,[a] Shek-Man Yiu,[a] Yun Chi [ID] *[a,c] and Kai Chung Lau [ID] *[a]

Homoleptic Ir(III) based carbene complexes are known to be the most promising emitters of future blue OLED devices. To provide the proof-of-concept, we designed a series of functional di-CF₃-functionalized benzo[*d*]imidazol-3-ium pro-chelates, which could afford single product emitters after proper modification. For benzoimidazol-2-ylidene with an *N*-methyl substituent, selective formation of the product can be achieved by introduction of *t*-butylphenyl for the phenyl group, as shown by shifting the product from mixed ***m*-Ir(dfp)₃** and ***f*-Ir(dfp)₃** to the single isomer ***f*-Ir(dfpb)₃**. Alternatively, for di-*N*-aryl substituted carbene chelates, the steric encumbrance imposed between the *ortho*-CF₃ group and the adjacent *N*-aryl substituent redirects the cyclometalation to the other *N*-aryl substituent, leading to the formation of one single product, *e.g.*, ***f*-Ir(tBpp)₃** and ***f*-Ir(ptBp)₃**. Moreover, the doped OLED based on ***f*-Ir(tBpp)₃** delivered true-blue emission centered at 457 nm and a maximum EQE of 15.6%. Furthermore, upon addition of terminal emitters ν-DABNA and *t*-DABNA, the respective hyper-OLEDs exhibited narrowband blue emission with a maximum EQE of 18.9% at 474 nm and 18.1% at 462 nm, respectively. These highlighted the potential of these Ir(III) emitters in the fabrication of blue OLEDs.

Introduction

Fluorination or incorporation of the perfluoroalkyl group to various functional materials has become an important methodology to enhance the performance of soft optoelectronic devices such as organic field-effect transistors (OFETs), light emitting transistors (OLETs) and light emitting diodes (OLEDs).[1–5] The specific features of such a fluorinated entity, *i.e.*, the trifluoromethyl (CF₃) group, are related to its high electron withdrawing character, together with enhanced hydrophobicity, lipophobicity and volatility. It is also known that the CF₃ group can lower the π-orbital energies of organic functional entities and materials.[6,7] The lowered energy levels facilitate electron injection, thus giving balanced carrier transportation and, hence, improved device efficiencies.[8–10] With this in mind, we decided to introduce the CF₃ group to Ir(III) based phosphors bearing functional imidazolylidene cyclometalates, with an attempt to further improve their photo- and electro-luminescence characteristics.

Similar manipulation has been documented in Ir(III) carbene complexes such as *m*-Ir(tfp_tz)₃[11–13] and its analogues.[14,15] Furthermore, Zysman-Colman and co-workers have also reported *mer*-arranged, homoleptic and blue Ir(III) phosphors comprising 1-methyl-3-(4-(trifluoromethyl)phenyl)-imidazol-2-ylidene chelates, *cf.*, *m*-Ir(tfpmi)₃ and its analogue.[16] Next, they switched to similar Ir(III) complexes containing a sterically demanding benzyl (or 2,4,6-trimethylbenzyl) appendage on carbene chelates, *cf.*, *m*-Ir(tfpi_Bn)₃.[17] One representative OLED device showed deep-blue electroluminescence with a peak maximum (λ_{max}) of 429 nm and CIE color coordinates of (0.16, 0.08), illustrating excellent performance for those with CF₃ substituted *N*-phenyl cyclometalating carbene chelates. However, their photoluminescence radiative rate constant (k_r) is in the region of ~10⁵ s⁻¹, suggesting the dominant ligand-centered ππ* transition characteristics in the excited state. These photophysical properties are inferior to

[a]Department of Materials Science and Engineering and Department of Chemistry, City University of Hong Kong, Kowloon 999077, Hong Kong SAR.
E-mail: yunchi@cityu.edu.hk, kaichung@cityu.edu.hk
[b]Department of Optoelectronics and Materials Technology, Taiwan Ocean University, Keelung 20224, Taiwan, China. E-mail: wenhung@mail.ntou.edu.tw
[c]Center of Super-Diamond and Advanced Films (COSDAF), City University of Hong Kong, Kowloon 999077, Hong Kong SAR

‡These authors contributed equally to this work.

This journal is © the Partner Organisations 2024

*Inorg. Chem. Front.*, 2024, **11**, 2413–2426 | **2413**

their Ir(III) based benzoimidazol-2-ylidene counterparts with an improved metal-to-ligand charge transfer (MLCT) character, which exhibited a much faster k_r of ~10^6 s^{-1}.[18] This opens up one possible research direction for improving both the photochemical and physical properties by increasing the MLCT contribution in the excited states of relevant Ir(III) carbene complexes.[18–20]

Accordingly, these desired properties can be achieved by expanding π-conjugation on the imidazol-2-ylidene (carbene) fragment and incorporating electron deficient entities at the same time.[18] One practical approach involved the replacement of the parent imidazolylidene with the benzo[d]imidazol-2-ylidene fragment,[21,22] followed by further conversion to imidazo[4,5-b]pyridin-2-ylidene,[23,24] imidazo[4,5-b]pyrazin-2-ylidene,[25–27] and even the purin-8-ylidene entity,[28,29] by addition of electro-negative nitrogen atom(s) at the designated skeletal position(s). Unlike the previously mentioned chelates and Ir(III) derivatives as shown in Scheme 1, these newly employed electron deficient carbene cyclometalates tended to afford two configurational isomers, e.g., m- and f-isomers under all conditions. Importantly, they showed structureless emission with a relatively fast radiative rate constant in solution at RT, confirming the dominant MLCT character in the excited state manifold.[30,31]

Herein, we report the design and preparation of such Ir(III) emitters bearing 4,6-bis(trifluoromethyl)-benzo[d]imidazol-2-ylidene cyclometalates. Their molecular structures are depicted in Scheme 2, in which m-/f-**Ir(dfp)₃**, f-**Ir(dfpb)₃**, f-**Ir(tBpp)₃** and f-**Ir(ptBp)₃** are associated with (i) either a phenyl or p-t-butyl-phenyl cyclometalating unit and (ii) a methyl, phenyl or p-t-butylphenyl peripheral appendage. To these designs, the trifluoromethyl (CF₃) group is expected to be inert to environmental perturbation and, thus, may demonstrate an increased chemical stability toward those offered by skeletal nitrogen atoms, which is known to be basic due to the possession of a lone pair of electrons. Not to mention that its ortho-CF₃ group can provide critical steric encumbrance to allow the selective formation of a certain favorable geometrical isomer, i.e., achieving selective synthesis of one isomer out of four statistically distributed products. Hence, tedious separation of isomers was no longer required, which is particularly important for the scale-up operation and marking an essential milestone in syntheses. Moreover, this site-selectivity is of uttermost importance to the widespread employment of di-aryl substituted benzoimidazol-2-ylidene and its analogues,[32–34] as they are deemed superior to their mono-N-aryl counterparts in serving as blue OLED emitters. However, the introduction of either 2,6- or 3,5-dialkylaryl substituents gave only decomposition, while using a 4-substituted aryl group afforded a mixture of up to four isomers,[35–37] confirming the success of the current strategy. Finally, fabrication of OLED devices was executed using three Ir(III) emitters f-**Ir(dfp)₃**, f-**Ir(tBpp)₃** and f-**Ir(ptBp)₃**. These emitters can serve as both the sole dopant and Förster Resonance Energy Transfer (FRET) sensitizer to
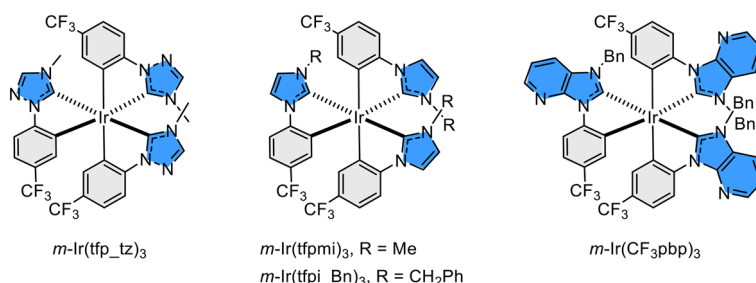
Scheme 1 Drawings of homoleptic Ir(III) carbene complexes bearing CF₃ substituted N-phenyl cyclometalates.
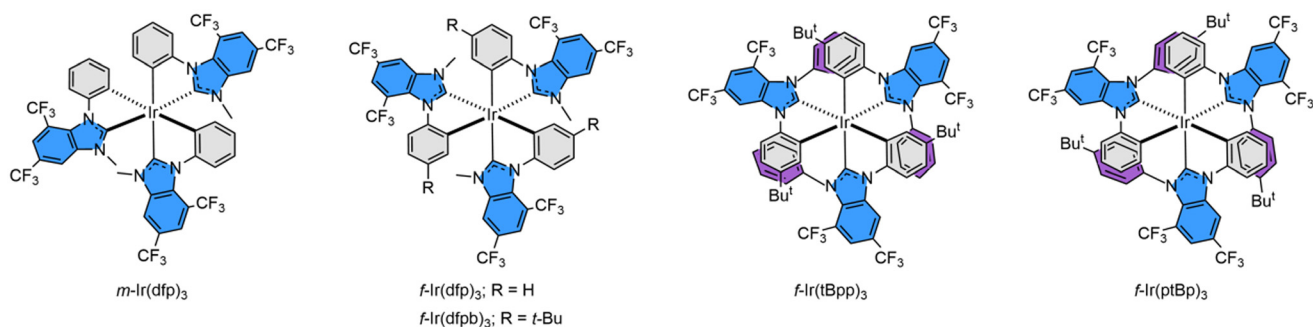
Scheme 2 Structural drawings of Ir(III) complexes bearing dual CF₃ substituted benzoimidazol-2-ylidene, confirming the selective cyclometalation of the N-aryl substituent.

2414 | *Inorg. Chem. Front.*, 2024, **11**, 2413–2426

This journal is © the Partner Organisations 2024

both the terminal emitters ν-DABNA and t-DABNA, in achieving narrow band true blue emission, as demanded by emerging industrial applications.

Results and discussion

Preparation and characterization

The functional 1-aryl-1H-benzo[d]imidazole with dual trifluoromethyl (CF$_3$) substituents was best synthesized using a multi-step protocol as depicted in Scheme 3. First, the key starting material 2-bromo-3,5-bis(trifluoromethyl)aniline (**A**) was prepared by bromination of commercially available 3,5-bis(trifluoromethyl)aniline using N-bromosuccinimide in CH$_2$Cl$_2$ at ~5 °C. After that, it was treated with a stoichiometric amount of triethyl orthoformate in the presence of glacial acetic acid as a catalyst at 120 °C, followed by the addition of aniline or 4-t-butylaniline at 140 °C. This two-step operation procedure is aimed at *in situ* preparation of functional ethyl N-arylformimidate as an intermediate,[38] which is expected to undergo further coupling with aniline to afford asymmetric N,N'-diarylformamidines with a 2-bromo-3,5-bis(trifluoromethyl)phenyl substituent.[39] After that, a copper-catalyzed intramolecular C–N bond coupling was executed to obtain the imidazole derivatives **B1** and **B2** in moderate yields,[40] following which N-alkylation with methyl trifluoromethanesulfonate has successfully afforded the anticipated 3-methyl-1-aryl-5,7-bis(trifluoromethyl)-1H-benzo[d]imidazol-3-ium pro-chelates **C1** and **C2** in high yields. Concurrently, according to the literature,[41] the reaction of **B1** and **B2** with diaryliodonium salt in DMF and with Cu(OAc)$_2$ as the catalyst afforded the respective di-N-aryl substituted pro-chelates **C3** and **C4** in high yields.

Isolation of these carbene pro-chelates made the preparation of all homoleptic Ir(III) carbene complexes an easy task. The iridium reagent [IrCl$_3$(tht)$_3$][42] was selected as the metal source due to its enhanced solubility in nonpolar aromatic solvents which is essential for the employment of sodium acetate as a catalyst.[43] Accordingly, treatment of pro-chelate **C1** with IrCl$_3$(tht)$_3$ and sodium acetate in refluxing t-butylbenzene (bp = 169 °C) afforded a mixture of both m- and f-isomers, namely **m-Ir(dfp)$_3$** and **f-Ir(dfp)$_3$**. In sharp contrast, treatment of respective pro-chelate **C2** with IrCl$_3$(tht)$_3$ afforded only the
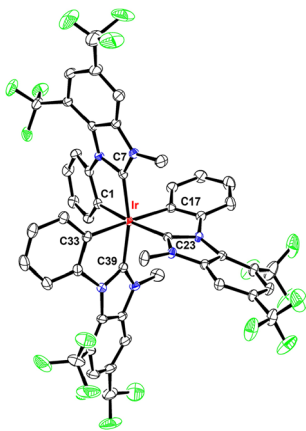
symmetric derivative **f-Ir(dfpb)$_3$** in refluxing t-butylbenzene. This could be attributed to the facile m- to f-isomerization process and greater thermodynamic stability for the f-isomer according to the literature.[44] Similarly, extensive heating of **C3** and **C4** with IrCl$_3$(tht)$_3$ in a higher boiling solvent 1,2,4-trichlorobenzene (bp = 214 °C) also afforded a single product **f-Ir(tBpp)$_3$** and **f-Ir(ptBp)$_3$**, respectively. The gross arrangement of chelates can be further confirmed by ^{1}H and ^{19}F NMR spectroscopy, which revealed a single set and three distinctive sets of resonance signals for the f- and m-isomers, respectively. Their structural drawings are depicted in Scheme 2 for scrutiny. For **f-Ir(ptBp)$_3$**, its structural assignment is confirmed by the observation of a total of four sets of doublet of doublets at δ 7.53 (dd, J = 8.4, 2.4 Hz), 7.36 (dd, J = 8.4, 2.4 Hz), 6.68 (dd, J = 8.0, 2.0 Hz) and 6.54 (dd, J = 8.0, 2.0 Hz) at room temperature, and the distinctive J_{HH} coupling constants of 8.4 and 2.4 Hz, 8.0 and 2.0 Hz were assigned for the ABXY spin coupling pattern, due to the hindered rotation of these t-butylphenyl appendages. Notably, in addition to the formation of solely the f-isomers for both **f-Ir(tBpp)$_3$** and **f-Ir(ptBp)$_3$**, the pro-chelates **C3** and **C4** possess two distinctive aryl groups which, in principle, have equal probability of undergoing metal cyclometalation in affording isomeric products. However, only the aryl group that is far away from the *ortho*-substituted CF$_3$ group underwent selective cyclometalation, leaving the adjacent aryl group as a free appendage, as shown in **f-Ir(tBpp)$_3$** and **f-Ir(ptBp)$_3$**. This enhanced selectivity is most probably caused by the steric encumbrance exerted between the CF$_3$ group at the 7-position and the adjacent 1-aryl group of the benzo[d]imidazol-2-ylidene entity, which is best explained by the X-ray structural data of **m-Ir(dfp)$_3$** (*vide infra*). Furthermore, the reversible C–H activation and cyclometalation of aryl appendages is also responsible for the selective formation of a single product in the presence of sodium acetate at elevated temperature.[45,46]

A single crystal X-ray diffraction study on **m-Ir(dfp)$_3$** and **f-Ir(tBpp)$_3$** was executed to confirm the coordination arrangement of chelates. Fig. 1 depicts a distorted octahedral structure of **m-Ir(dfp)$_3$**, as expected for the *mer*-configuration. Six Ir–C distances were found to be different, among which all Ir–C$_{(carbene)}$ distances (Ir–C7 = 2.006(3), Ir–C23 = 2.047(3) and Ir–C39 = 2.021(3) Å) are notably shorter than the corresponding Ir–C$_{(aryl)}$ distances (Ir–C1 = 2.076(3), Ir–C17 = 2.112(3), and Ir–C33 = 2.104(3) Å).
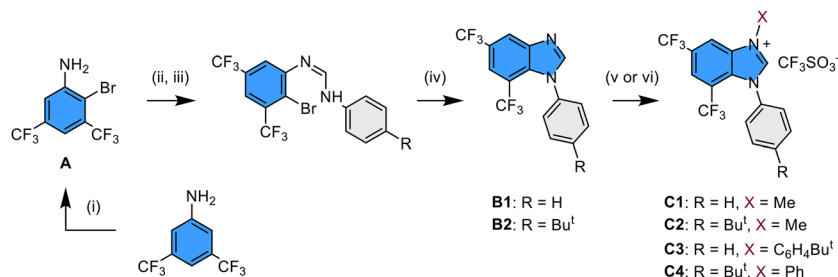
**Scheme 3** Synthetic protocols to the functional benzo[d]imidazol-3-ium pro-chelates: (i) NBS, DCM, 0 °C; (ii) triethyl orthoformate, glacial acetic acid, 120 °C; (iii) arylamine, 140 °C; (iv) DBU, CuI, DMSO, 150 °C; (v) CF$_3$SO$_3$Me, toluene, RT; (vi) diaryliodonium salt, Cu(OAc)$_2$·H$_2$O, DMF, 110 °C.

This journal is © the Partner Organisations 2024

Inorg. Chem. Front., 2024, **11**, 2413–2426 | **2415**

Fig. 1 Structure drawing of *m*-**Ir(dfp)₃** with thermal ellipsoids shown at the 30% probability level. Selected bond length (Å): Ir–C1 = 2.076(3), Ir–C7 = 2.006(3), Ir–C17 = 2.112(3), Ir–C23 = 2.047(3), Ir–C33 = 2.104(3), and Ir–C39 = 2.021(3). Selected bond angle (°): C1–Ir–C23 = 169.91(10), C7–Ir–C39 = 166.42(10), and C17–Ir–C33 = 177.97(11).

Particularly, the unique Ir–C1 vector, that is uniquely located *trans* to the Ir–C$_{(carbene)}$ vector, is the shortest among all Ir–C$_{(aryl)}$ vectors, showing the reduced *trans*-effect of carbene in reference to the aryl entities. Concurrently, the Ir–C23 distance of the same carbene chelate is also longer than the other two, *trans*-arranged Ir–C$_{(carbene)}$ fragments, showing the relatively strengthened *trans*-effect exerted by its opposite phenyl cyclometalate. Furthermore, the distances of this *trans*-arranged C$_{(aryl)}$–Ir–C$_{(carbene)}$ vector of **m-Ir(dfp)₃** are comparable to the respective C$_{(aryl)}$–Ir–C$_{(carbene)}$ distances observed in *f*-coordinated ***f*-Ir(tBpp)₃**, *i.e.*, with Ir–C19 = 2.0903(19) and Ir–C13 = 2.0428(17) Å, as depicted in Fig. 2. These results confirmed the variation of
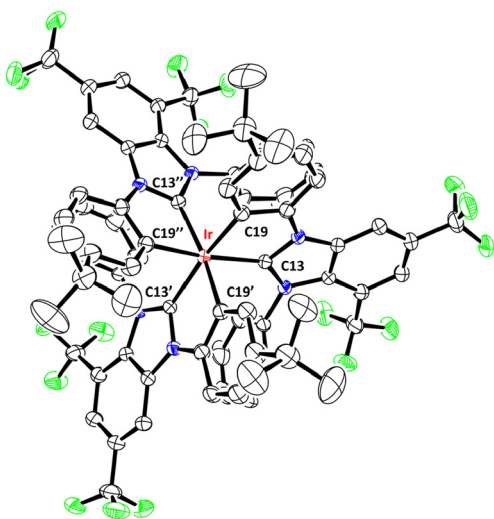
Fig. 2 Structure drawing of *f*-**Ir(tBpp)₃** with thermal ellipsoids shown at the 30% probability level. Selected bond length (Å): Ir–C13 = 2.0428(17) and Ir–C19 = 2.0903(19). Selected bond angles (°): C13–Ir–C19′ = 168.52(8).

Ir–C distances in response to their local coordinative environment.

Notably, there existed a large angular distortion between the imidazolylidene entity and phenyl cyclometalate of each individual carbene chelates of **m-Ir(dfp)₃**, which is obviously caused by the steric hindrance exerted by the CF₃ group at the 7-position and adjacent 1-phenyl cyclometalate. The averaged torsional angle is calculated to be around 23°, which is notably larger than the 14° distortion observed in ***f*-Ir(tBpp)₃**, and the 7-position is occupied by a smaller hydrogen atom instead. Hence, this angular distortion will be a major driving force in giving the structural selectivity as observed in Ir(III) complexes ***f*-Ir(tBpp)₃** and ***f*-Ir(ptBp)₃**. Furthermore, the closest contacts between the CF₃ group and the *ortho* C–H entity of the adjacent phenyl cyclometalate in **m-Ir(dfp)₃** were found to be in the range of 2.306–2.355 Å, which are shorter than the sum of the van der Waals radii of hydrogen (1.2 Å) and fluorine (1.47 Å) and validated the repulsive interaction.

Photophysical measurement

Fig. 3 depicts the UV-Vis absorption and emission spectra of the studied Ir(III) complexes in toluene and degassed toluene, and the respective numerical data are summarized in Table 1. Generally speaking, all Ir(III) complexes exhibit multiple high energy bands beyond 320 nm, which can be assigned to ligand-centered $\pi\pi^*$ and/or ligand-to-ligand charge transfer (LLCT) transitions.[47] Notably, *f*-isomers show an additional, strong absorption band centered at ~370 nm, and the pattern has been observed for many *f*-arranged Ir(III) carbene complexes documented in the literature, while **m-Ir(dfp)₃** exhibits a much weaker absorption band within this region; however, its peak onset was further extended to a longer wavelength of ~440 nm. This was not observed for their *f*-counterpart, manifesting a relatively lower energy MLCT transition character.

For photoluminescence, ***f*-Ir(dfb)₃** and ***f*-Ir(dfpb)₃** exhibit true blue emission with a peak maximum located at 462 and 472 nm, and this difference in peak wavelength is obviously induced by the *t*-butyl substituent in the phenyl
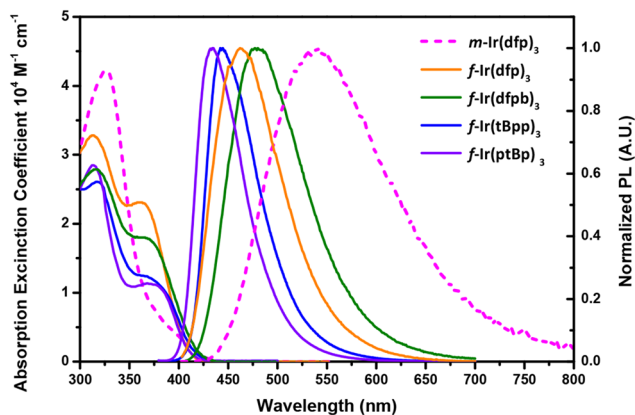
Fig. 3 Absorption and emission spectra of the studied Ir(III) carbene complexes in degassed toluene at RT.

2416 | *Inorg. Chem. Front.*, 2024, **11**, 2413–2426

This journal is © the Partner Organisations 2024

Table 1 Photophysical data of the studied Ir(III) carbene complexes in toluene

	Abs λ_{max}/nm; ε $(10^4\ M^{-1}\ cm^{-1})^a$	Em λ_{max}^b (nm)	FWHM^c (nm eV^{-1})	$\Phi^{b,d}$ (%)	τ_{obs}^b (μs)	τ_{rad} (μs)	k_r $(10^5\ s^{-1})$	k_{nr} $(10^5\ s^{-1})$
m-Ir(dfp)₃	327 (4.22), 381 (0.55)	541	149/0.59	11.1	0.18	1.64	6.1	48.5
f-Ir(dfp)₃	314 (3.28), 362 (2.31)	462	84/0.46	64.3	0.85	1.33	7.5	4.2
f-Ir(dfpb)₃	316 (2.79), 369 (1.78)	472	83/0.47	62.0	0.9	1.45	6.8	4.2
f-Ir(tBpp)₃	318 (2.61), 372 (1.21)	444	60/0.36	78.9	0.98	1.24	8.1	2.2
f-Ir(ptBp)₃	314 (2.85), 372 (1.13)	435	55/0.35	60.7	0.85	1.40	7.1	4.6

^{a} Those were recorded in toluene at a concentration of 10^{-5} M at RT. ^{b} Those were recorded in degassed toluene at a concentration of 10^{-5} M at RT. ^{c} Full width at half maximum. ^{d} Coumarin 153 (C153) in ethanol (Q.Y. = 58% and λ_{max} = 530 nm) and Coumarin 102 (C102) in methanol (Q.Y. = 80% and λ_{max} = 480 nm) were employed as standards.

cyclometalates.[27,28] The same trend was observed by comparison between **f-Ir(tBpp)₃** (444 nm) and **f-Ir(ptBp)₃** (435 nm) as the former possesses a *t*-butyl substituent at the cyclometalating sites. Interestingly, these two complexes with di-*N*-aryl substituted chelates display both a more blue-shifted emission peak wavelength and a narrowed emission band with a FWHM of <60 nm, showing the reduced influence from solvation. Moreover, the observed peak wavelength between **f-Ir(dfp)₃** and **f-Ir(ptBp)₃** is related to both the dislocated CF₃ groups on the benzoimidazol-2-ylidene chelate and the replacement of *N*-methyl with an *N*-aryl appendage. In fact, our DFT data are also in agreement with this hypothesis (*vide infra*). Most importantly, complexes with facial configurations exhibit a high quantum yield of 60.3–78.9% and a short radiative lifetime between 1.24 μs and 1.45 μs under the same measurement conditions, confirming their potential in fabricating efficient OLED devices. In contrast, as the only *mer*-derivative of this family, **m-Ir(dfp)₃** exhibits broader and red-shifted emission and a lower photoluminescence quantum yield (PLQY) of 11.1%, which can be rationalized by much enhanced solvation.[24] Furthermore, the emission of all studied Ir(III) complexes with a concentration of 2 wt% doped in PMMA was measured and is summarized in Fig. S1† and Table 2. The emission peak in PMMA of **m-Ir(dfp)₃** is blue shifted by 42 nm compared to that recorded in toluene, confirming the reduction of solvation. In contrast, all *f*-complexes showed red-shifted emission and no notable change in bandwidth at the same time, confirming their good photophysical properties in both the solution and thin film states.

Table 2 Photophysical data of the studied Ir(III) carbene complexes as solid-state thin films at RT

	Em λ_{max}^a (nm)	$\Phi^{a,b}$ (%)	$\tau_{obs}^{a,b}$ (μs)	$\tau_{rad}^{a,b}$ (μs)	FWHM^c (nm eV^{-1})
m-Ir(dfp)₃	499	41	0.68	1.66	112/0.54
f-Ir(dfp)₃	466	59	1.14	1.94	86/0.48
f-Ir(dfpb)₃	474 [468]	68 [78]	1.20 [1.53]	1.77 [1.96]	88/0.47
f-Ir(tBpp)₃	452 [461]	80 [85]	1.08 [1.30]	1.35 [1.53]	62/0.37
f-Ir(ptBp)₃	438 [449]	65 [78]	0.94 [1.33]	1.45 [1.86]	52/0.33

^{a} PL spectrum, quantum yield and lifetime were recorded in the doped PMMA thin film at RT (2 wt%) using an integration sphere. ^{b} Data in square brackets were measured in the co-doped PPT host (20 wt%). ^{c} Full width at half maximum.

Electrochemical and thermal characterization

Cyclic voltammetry was measured in acetonitrile solution at RT (Fig. S2†). As expected, oxidation mainly occurred at the Ir(III) metal center, with the oxidation onset potentials of *f*-isomers occurring in the region of 0.52–0.64 V (*vs.* Fc/Fc⁺), while that of **m-Ir(dfp)₃** exhibited a cathodic shift to 0.30 V, which was consistent with its red shifted emission spectrum. Complexes **m-Ir(dfp)₃**, **f-Ir(dfp)₃** and **f-Ir(dfpb)₃** show irreversible oxidation processes with the anodic onset potentials at 0.30, 0.64, and 0.58 V, respectively, while complexes **f-Ir(tBpp)₃** and **f-Ir(ptBp)₃** showed quasi-reversible oxidation peaks with the anodic onset potentials at 0.52 and 0.64 V, respectively. It seems that the pendent *N*-aryl group had also improved the reversibility to the oxidized complexes. Alternatively, all these Ir(III) complexes presented irreversible reduction peaks spanning from −2.44 to −2.33 V. Thermogravimetric data were then recorded and are given in Fig. S3 and Table S1.† As can be seen, **f-Ir(tBpp)₃** appeared to exhibit the lowest decomposition temperature (T_d) of 292 °C, while others displayed excellent thermal stability with a T_d well above 345 °C. Interestingly, all these emitters can be purified by vacuum sublimation with the operational temperature being ∼60 °C lower than their T_d, indicating that the CF₃ group has greatly improved their volatility and enables the fabrication of OLED devices *via* more convenient vacuum deposition processes.

Theoretical investigation

The lowest singlet (S_1) and triplet (T_1) excited states for the studied Ir(III) complexes were investigated by TD-DFT calculations[48,49] to gain an understanding of the nature of the absorption/emission bands and the effect of chelate modification on their photophysical properties. The details of computational methods are described in the ESI.†

The vertical excitation energies of the $S_0 \rightarrow S_1$ transition were calculated to be 438, 389, 395, 401 and 394 nm for **m-Ir(dfp)₃**, **f-Ir(dfp)₃**, **f-Ir(dfpb)₃**, **f-Ir(tBpp)₃** and **f-Ir(ptBp)₃**, respectively (Table 3), which are correlated with their experimental lowest-energy absorption tails around 400 nm (Fig. 3). The calculated vertical excitation energies for the $S_0 \rightarrow T_1$ transition, which is usually used to represent the $T_1 \rightarrow S_0$ emission in the equilibrium structure of S_0, were 451, 419, 424, 431 and 416 nm for **m-Ir(dfp)₃**, **f-Ir(dfp)₃**, **f-Ir(dfpb)₃**, **f-Ir(tBpp)₃** and **f-Ir(ptBp)₃**, respectively (Table 3). These values are comparable to

Table 3 Calculated E_{HOMO}, HOMO–LUMO (H–L) gap, vertical excitation energy (λ) and oscillator strength (f) of the lowest singlet (S_1) and triplet (T_1) excited states, main orbital transition contributions of the $S_0 \rightarrow S_1/T_1$ excitation processes, and assignment of $S_0 \rightarrow T_1$ excitation transition at their geometries optimized for the ground state (S_0)

	$E_{HOMO}{}^a$ (eV)	H–L gap^a (eV)	Excitation	λ^b [nm eV^{-1}]	f^b	MO contribution (>20%)^b	Assignment^c					Sum contribution^d
							MLCT	ILCT	LC	LMCT	MC	
m-Ir(dfp)$_3$	−5.45	3.44	$S_0 \rightarrow T_1$	451/2.75	0	HOMO → LUMO (72.3%)	35.8%	37.9%	18.4%	4.9%	3.1%	87.2%
			$S_0 \rightarrow S_1$	438/2.83	0.0010	HOMO → LUMO (84.7%)						
f-Ir(dfp)$_3$	−5.67	3.80	$S_0 \rightarrow T_1$	419/2.96	0	HOMO → LUMO (77.6%)	30.7%	38.0%	26.0%	3.6%	1.7%	90.9%
			$S_0 \rightarrow S_1$	389/3.18	0.0182	HOMO → LUMO (86.5%)						
f-Ir(dfpb)$_3$	−5.57	3.70	$S_0 \rightarrow T_1$	424/2.92	0	HOMO → LUMO (77.7%)	30.0%	38.8%	25.7%	3.8%	1.7%	90.7%
			$S_0 \rightarrow S_1$	395/3.14	0.0927	HOMO → LUMO+1 (91.8%)						
f-Ir(tBpp)$_3$	−5.50	3.67	$S_0 \rightarrow T_1$	431/2.98	0	HOMO → LUMO (79.0%)	28.1%	45.1%	22.6%	3.0%	1.2%	92.8%
			$S_0 \rightarrow S_1$	401/3.10	0.0053	HOMO → LUMO (94.0%)						
f-Ir(ptBp)$_3$	−5.58	3.77	$S_0 \rightarrow T_1$	416/2.98	0	HOMO → LUMO (81.0%)	32.6%	36.5%	25.3%	3.7%	1.9%	90.7%
			$S_0 \rightarrow S_1$	394/3.14	0.0552	HOMO → LUMO+1 (95.9%)						

^{a} The E_{HOMO} and H–L gap are computed at optimized S_0 structures at the B3LYP-D3(BJ)/def2-SVP level with the polarizable continuum model (PCM) for toluene. ^{b} The results were calculated using TD-DFT using the B3LYP functional with PCM for toluene (cf., ESI†). ^{c} The percentages of all $S_0 \rightarrow T_1$ excitation character were calculated using the IFCT(Hirshfeld) method. ^{d} The sum contribution is MLCT + ILCT + LC − LMCT.

the experimental phosphorescence (λ_{max}^{PL} = 541, 462, 472, 444 and 435 nm in toluene; λ_{max} = 499, 466, 474, 452 and 438 nm in the doped PMMA thin film, respectively; see Fig. 3, Tables 1 and 2) with a MAD (mean absolute deviation) of about ≈0.25 eV (≈5.7 kcal mol^{-1}) in toluene. Moreover, the calculated adiabatic emission energy (565, 456, 459, 441 and 424 nm, Table 4) is much closer to the experimental wavelengths in toluene with a smaller MAD (0.06 eV or 1.4 kcal mol^{-1}).

To further understand the emission properties of the studied Ir(III) complexes, the natural transition orbital (NTO) analysis[50] to express the $S_0 \rightarrow T_1$ transition as a single pair of orbitals was applied. The predominant NTO pairs found for the $S_0 \rightarrow T_1$ transition are present in Fig. 4. For all the four

Table 4 Calculated adiabatic and vertical $T_1 \rightarrow S_0$ transition energy, radiative lifetime (τ_{rad}), and radiative rate (k_r) of m-Ir(dfp)$_3$, f-Ir(dfp)$_3$, f-Ir(dfpb)$_3$, f-Ir(tBpp)$_3$, and f-Ir(ptBp)$_3$

Emission ($T_1 \rightarrow S_0$)	λ^a [nm eV^{-1}]	λ^b [nm eV^{-1}]	$\tau_{rad}{}^c$ (μs)	$k_r{}^c$ (μs^{-1})
m-Ir(dfp)$_3$	565/2.20	447/2.77	0.23/0.38	4.30/2.64
		(*822/1.51*)	(*1.55/1.94*)	(*0.65/0.52*)
f-Ir(dfp)$_3$	456/2.72	407/3.05	1.02/1.35	0.98/0.74
		(*830/1.50*)	(*6.18/6.87*)	(*0.16/0.15*)
f-Ir(dfpb)$_3$	459/2.70	417/2.97	0.84/1.11	1.20/0.90
		(*772/1.61*)	(*5.89/5.99*)	(*0.17/0.16*)
f-Ir(tBpp)$_3$	441/2.81	428/2.90	0.44/0.45	2.27/2.24
		(*520/2.38*)	(*1.37/1.52*)	(*0.73/0.66*)
f-Ir(ptBp)$_3$	424/2.92	415/2.99	1.11/1.23	0.90/0.82
		(*489/2.54*)	(*1.09/1.16*)	(*0.91/0.86*)

^{a} The adiabatic emission energy was obtained from the difference between the optimized structures of S_0 and T_1 states using the B3LYP functional with a polarizable continuum model (PCM) for toluene (cf. ESI†). ^{b} The vertical emission energy between S_0 and T_1 states was obtained using the SOC-TDDFT method in ORCA at optimized structures of S_0 (in normal font) and T_1 (in italic and bold fonts in parentheses). ^{c} The τ_{rad} and k_r are calculated by the arithmetic average/ Boltzmann average (at 298 K) of the SOC substates of T_1, at the optimized structures of S_0 (in normal font) and T_1 (in italic and bold fonts in parentheses).

facial Ir(III) complexes, namely f-Ir(dfp)$_3$, f-Ir(dfpb)$_3$, f-Ir(tBpp)$_3$ and f-Ir(ptBp)$_3$, the occupied NTOs are delocalized at both the Ir(III) metal center and cyclometalating carbene chelates (in π orbitals); while the virtual NTOs are mainly localized at the carbene donor fragments (in π* orbitals). Only for the meridional complex (m-Ir(dfp)$_3$), the occupied NTO is delocalized at the Ir(III) metal center and carbene chelates whereas the virtual NTO is localized at the N-aryl cyclometalates. It indicates that for m-Ir(dfp)$_3$, the overlaps between the occupied and virtual NTOs are greatly reduced and lead to a diminished ligand-centered (LC) character in the $S_0 \rightarrow T_1$ transition.

Although the NTO analysis makes use of the dominant molecular orbital pairs, the contribution of the NTO pairs is unable to reveal the full properties of $S_0 \rightarrow T_1$ excitation. In fact, no obvious difference is found between the NTO analysis and TD-DFT results, for example, the calculated eigenvalues of the NTOs for the $S_0 \rightarrow T_1$ transition of f-Ir(dfp)$_3$ is 0.824 (Fig. 4), representing that 82.4% of $S_0 \rightarrow T_1$ excitation is contributed by the "HOMO → LUMO" transition, and the results are similar to the TD-DFT value of 77.6% (Table 3).
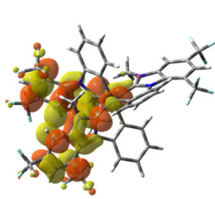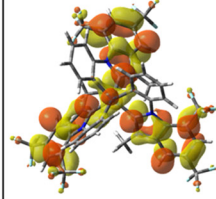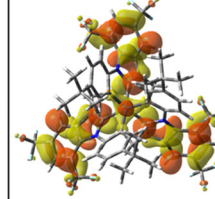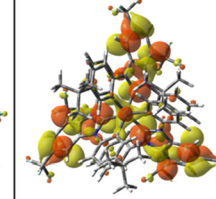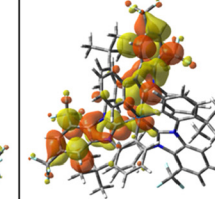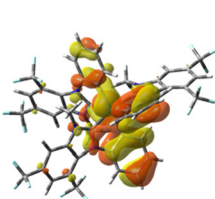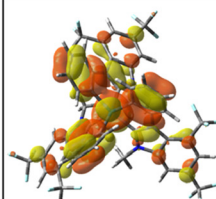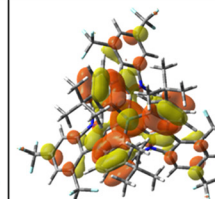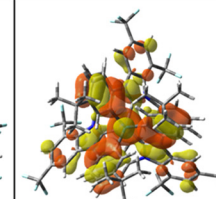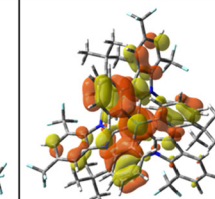
The inter-fragment charge transfer (IFCT) method, available from the Multiwfn software package,[51] was employed to quantify the contributions of relevant molecular orbitals (MOs) to the selected electronic transition. This manipulation is to provide a better picture of the $S_0 \rightarrow T_1$ transition, and the percentage of MLCT, intra-ligand charge transfer (ILCT), ligand-centered (LC), ligand-to-metal charge transfer (LMCT) and metal-centered (MC) dd contributions are depicted in Table 4. Based on the IFCT analysis, the effect of ligand modification on k_r is summarized as follows: (i) m-Ir(dfp)$_3$ has the highest percentage of MCLT (35.8%), LMCT (4.9%) and MC (3.1%) among all studied Ir(III) complexes. It also features the lowest percentage of LC (18.4%), which is consistent with the lowest orbital overlaps between the occupied and virtual NTOs of m-Ir(dfp)$_3$ (Fig. 4). (ii) When the meridional m-Ir(dfp)$_3$ is changed to its facial isomer f-Ir(dfp)$_3$ (Scheme 2), the MLCT character (30.7%) is reduced by 5.1%, the LMCT and MC characters are

2418 | *Inorg. Chem. Front.*, 2024, **11**, 2413–2426

This journal is © the Partner Organisations 2024

Fig. 4 Natural transition orbital (NTO) pairs expressing the $S_0 \rightarrow T_1$ excitation of the studied Ir(III) complexes at their geometries optimized for the ground state, with the contribution of dominant molecular orbitals (MOs) to NTOs provided.

also slightly reduced whereas the LC character is greatly increased from 26.0% to 33.6%. The increased LC character also manifests on the orbital overlaps of NTO analysis on *f*-**Ir(dfp)₃** (Fig. 4). (iii) Replacing the *N*-phenyl cyclometalate of carbene chelate with the 4-(*t*-butyl)phenyl group of *f*-**Ir(dfpb)₃** does not impose any significant effect on the MLCT, ILCT, LC and LMCT character. This suggests that both *f*-**Ir(dfpb)₃** and *f*-**Ir(dfp)₃** should have similar photophysical properties. (iv) Upon changing the dual CF_3 substituents (from the 1,3-position to the 2,4-position) and changing the *N*-methyl appendages to phenyl groups (Scheme 2, from *f*-**Ir(dfpb)₃** to *f*-**Ir(tBpp)₃**), the ILCT character is greatly increased to 45.1%, being the highest ILCT percentage observed among all complexes. The modification of chelates in this step may reduce the steric hindrance and result in more effective ILCT character of *f*-**Ir(tBpp)₃**. The LMCT character (3.0%) of *f*-**Ir(tBpp)₃** is also the smallest one among all complexes. (v) Alternately, simultaneous replacement of both the 4-(*t*-butyl)phenyl cyclometalate and the *N*-phenyl appendage on *f*-**Ir(tBpp)₃** with the phenyl cyclometalate and 4-(*t*-butyl)phenyl appendage gives *f*-**Ir(ptBp)₃** (Scheme 2). The ILCT character of *f*-**Ir(ptBp)₃** becomes lower (36.5%), but its MLCT and LC characters are increased slightly. The percentages of MLCT (32.6%), ILCT (36.5%) and LC (25.3%) characters of *f*-**Ir(ptBp)₃** are akin to those of *f*-**Ir(dfp)₃** and *f*-**Ir(dfpb)₃**.

The IFCT method suggests that the $S_0 \rightarrow T_1$ excitation exhibits a dominant mixture of MLCT, ILCT and LC characters for all the four facial Ir(III) complexes. For the solely meridional complex (*m*-**Ir(dfp)₃**), the $S_0 \rightarrow T_1$ excitation mainly consists of mixed MLCT and ILCT character, with a relatively smaller LC character. The respective sum contribution (Table 3) of "MLCT + ILCT + LC–LMCT" of 87.2%, 90.9%, 90.7%, 92.8% and 90.7% for *m*-**Ir(dfp)₃**, *f*-**Ir(dfp)₃**, *f*-**Ir(dfpb)₃**, *f*-**Ir(tBpp)₃** and *f*-**Ir(ptBp)₃** correlates excellently with the respective measured k_r

values (in μs^{-1}, Table 1) of 0.61, 0.75, 0.68, 0.81 and 0.71 from experimental measurements. Based on the IFCT method, it appears that the meridional complex (*m*-**Ir(dfp)₃**, 87.2%) has the smallest radiative decay rate while the facial complex of *f*-**Ir(tBpp)₃** has the fastest radiative decay rate (92.8%).

Following the IFCT prediction, we perform calculations to investigate the theoretical τ_{rad} and k_r. The emission energy calculated for the optimized structure (T_1) might have a physical meaning, since phosphorescence is a long-lived process such that it may give the emitting species enough time to relax from the triplet manifold to a lower energy geometry. However, it has been pointed out that although a lot of calculations using the optimized structure (T_1) can give good prediction to the experimental τ_{rad}, many other works of τ_{rad} using the ground state geometry (S_0) also present a better correlation with the experimental data.[52–54] As the "actual" emitting species sit between the ground state (S_0) and excited state (T_1) levels,[55,56] we here apply the spin–orbit coupling (SOC)-TDDFT method on both the optimized S_0 and T_1 structures for the estimation of τ_{rad} and k_r.

The calculated emission energies, τ_{rad} and k_r at both optimized S_0 and T_1 geometries, are summarized in Table 4, and the results obtained using the arithmetic average or Boltzmann average of the SOC substates are similar. Here, we focus on the arithmetic average results. (i) For the $T_1 \rightarrow S_0$ emission of *m*-**Ir(dfp)₃**, the calculated τ_{rad} is 0.23 μs (at the S_0 structure) and 1.55 μs (at the T_1 structure). In comparison with the experimental τ_{rad} (1.64 μs, Table 1), the true emitting intermediate of *m*-**Ir(dfp)₃** is suggested to be closer to the T_1 structure. (ii) Unlike the emission of *m*-**Ir(dfp)₃**, the experimental τ_{rad} (1.33 μs) of its facial isomer *f*-**Ir(dfp)₃** is closer to the calculated τ_{rad} of 1.02 μs (in the S_0 geometry), suggesting that the true emitting intermediate of *f*-**Ir(dfp)₃** is near to the S_0 structure. (iii) A similar conclusion can also be drawn for *f*-**Ir**

This journal is © the Partner Organisations 2024

Inorg. Chem. Front., 2024, **11**, 2413–2426 | **2419**

(dfpb)₃, in which the true emitting intermediate is near to the S_0 structure. The calculated τ_{rad} of 0.84 μs (in the S_0 structure) is much closer to the experimental τ_{rad} (1.45 μs) than the calculated τ_{rad} (5.89 μs) based on the T_1 structure. (iv) For ***f*-Ir(tBpp)₃**, the experimental τ_{rad} of 1.24 μs deviates from the calculated τ_{rad} of 0.44 μs (in the S_0 structure) and 1.37 μs (in the T_1 structure) by +0.80 and −0.13 μs, respectively. We suggested that the actual emitting intermediate of ***f*-Ir(tBpp)₃** resembles both S_0 and T_1 structures. (v) The calculated τ_{rad} values of 1.11 μs (in the S_0 geometry) and 1.09 μs (in the T_1 geometry) of ***f*-Ir(ptBp)₃** are almost the same, hinting that its emitting intermediate resembles both the S_0 and T_1 structures. It is worth noting here that the uncertainty (∼1.7 μs) of τ_{rad} for other Ir(III) complexes predicted with the SOC-TDDFT method is relatively large.[57] From the above analysis, we conclude that the phosphorescence process of all the four facial Ir(III) complexes likely occurred near the S_0 structure while that of the meridional complex (***m*-Ir(dfp)₃**) is initiated in the T_1 structure.

Device performance

To examine the electroluminescence (EL) characteristics, we chose ***f*-Ir(dfpb)₃**, ***f*-Ir(tBpp)₃** and ***f*-Ir(ptBp)₃** as sensitizers for constructing both phosphorescent and hyper-OLED devices. Phosphorescent OLEDs are known to offer the full utilization of all excitons generated during operation, while hyper-OLEDs exhibit another capacity to further improve efficiency by transferring energy from sensitizers to fluorescent emitters.[58–62]

The adjustable emission energy, enhanced spin–orbit coupling, and a greater MLCT fraction designate these Ir(III) carbene emitters as promising candidates for realizing effective FRET.[37,63–68] The respective phosphorescent and hyper-OLEDs were constructed using the device structure: indium tin oxide (ITO)/4 wt% rhenium oxide (ReO₃): *N,N*-dicarbazolyl-3,5-benzene (mCP) (60 nm)/mCP (15 nm)/EML (20 nm)/tris-[3-(3-pyridyl)mesityl]borane (3TPYMB) (50 nm)/ lithium 8-hydroxyquinolinolate (Liq) (0.5 nm)/Al (100 nm). This configuration, previously detailed in our earlier study, is illustrated in Fig. 5a.[69] The hole-transport layer (HTL) and electron-transport layer (ETL) consisted of mCP and 3TPYMB, respectively. Thin layers of 4 wt% ReO₃ doped mCP and Liq were also applied to enhance the carrier and charge injection from the respective electrodes.[70] The emissive layer (EML) contained 20 wt% Ir(III) metal phosphors (***f*-Ir(dfpb)₃**, ***f*-Ir(tBpp)₃** and ***f*-Ir(ptBp)₃**) and additional 1 wt% terminal emitters (*ν*-DABNA and *t*-DABNA) for hyper-OLEDs incorporated into the host material, 2,8-bis(diphenylphosphoryl)dibenzo[*b,d*]thiophene (PPT).[71,72] Their EL characteristics are presented in Fig. 5 (and Fig. S4 and S5 of the ESI†), together with the pertinent parameters that are consolidated in Table 5.

To confirm our device design, the EL characteristics were explored without the addition of an MR-TADF terminal emitter. These devices displayed a progressive hypsochromic shift from sky blue to blue with peak maxima at 481, 457, and 453 nm for ***f*-Ir(dfpb)₃**, ***f*-Ir(tBpp)₃** and ***f*-Ir(ptBp)₃**, respectively.
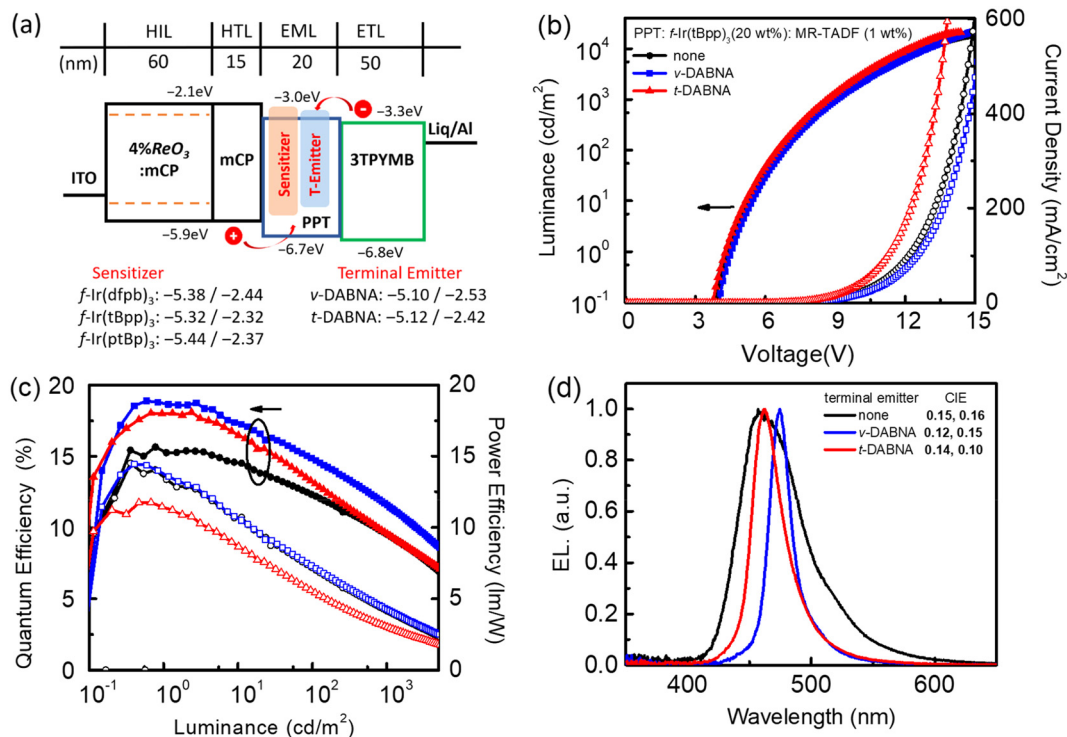
Fig. 5 (a) The energy diagram of all OLED and hyper-OLED devices fabricated in this study, (b) current density–voltage–luminance (*J*−*V*−*L*) characteristics of devices fabricated using ***f*-Ir(tBpp)₃** as a dopant, and devices with **Ir(tBpp)₃** as a sensitizer, together with *ν*-DABNA and *t*-DABNA as terminal emitters, and (c) respective EQE and PE diagrams as a function of luminance, and (d) EL spectra.

2420 | *Inorg. Chem. Front.*, 2024, **11**, 2413–2426

This journal is © the Partner Organisations 2024

Table 5 Characteristics of OLED devices using phosphorescent dopants and corresponding hyper-OLEDs with terminal emitters ν-DABNA and t-DABNA

Sensitizer	1 wt% T-emitter	V_{on} [V]	EQE/CE/PE at max. [%/cd A^{-1}/lm W^{-1}]	EQE/CE/PE at 10^3 cd m^{-2} [%/cd A^{-1}/lm W^{-1}/V]	λ_{max} [nm]	FWHM [nm]	CIE $[x,y]$
f-Ir(dfpb)$_3$	None	4.5	10.6/20.4/12.0	5.7/10.9/3.4/10.0	481	81	0.17, 0.29
	ν-DABNA	4.7	14.3/17.7/10.3	7.2/8.9/2.7/10.5	475	21	0.12, 0.19
	t-DABNA	4.7	14.3/14.2/9.2	4.5/4.5/1.4/10.1	466	30	0.13, 0.12
f-Ir(tBpp)$_3$	None	3.9	15.6/19.2/14.5	9.6/11.7/4.2/8.8	457	58	0.15, 0.16
	ν-DABNA	3.9	18.9/20.1/14.4	11.6/12.4/4.4/9.0	474	19	0.12, 0.15
	t-DABNA	3.8	18.1/15.7/11.7	9.7/8.4/3.1/8.6	462	29	0.14, 0.10
f-Ir(ptBp)$_3$	None	3.9	12.9/11.5/8.6	6.5/5.8/2.1/8.7	453	57	0.15, 0.10
	ν-DABNA	3.9	16.3/15.1/11.3	9.4/8.7/3.3/8.4	473	20	0.12, 0.13
	t-DABNA	3.9	14.1/11.9/8.1	5.19/4.39/1.31/9.5	461	33	0.14, 0.10

They were also accompanied by a decrease of full width at half maximum (FWHM) from 81 nm, 58 nm and to 51 nm, aligning well with their photoluminescence (PL) spectra (Table 1). In comparison to the devices with f-Ir(dfpb)$_3$ and f-Ir(tBpp)$_3$, the third device with f-Ir(ptBp)$_3$ demonstrated slightly superior chromaticity coordinates CIE$_{x,y}$ of 0.15 and 0.10 for deep-blue emission. On the other hand, the device based on f-Ir(tBpp)$_3$ demonstrated the highest efficiency, displaying a maximum external quantum efficiency (EQE$_{max}$) of 15.6%, a maximum current efficiency (CE$_{max}$) of 19.2 cd A^{-1}, and a maximum power efficiency (PE$_{max}$) of 14.5 lm W^{-1}. Conversely, relatively inferior efficiencies, $i.e.$, EQE$_{max}$, CE$_{max}$, and PE$_{max}$ values of 10.6%, 20.4 cd A^{-1}, and 12.0 lm W^{-1} and 12.9%, 11.5 cd A^{-1}, and 8.6 lm W^{-1} were observed for f-Ir(dfpb)$_3$ and f-Ir(ptBp)$_3$, respectively. The efficiencies seemed to follow the photoluminescence quantum yield (Φ_{PL}) recorded in toluene solution (Table 1) and both the PMMA polymer matrix and PPT host material (Table 2), while f-Ir(tBpp)$_3$ exhibits a faster radiative lifetime among the three studied Ir(III) complexes.

With the objective of achieving deep-blue hyper-OLEDs, a low concentration of MR-TADF terminal emitters (ν-DABNA and t-DABNA) was next incorporated into the EML. Fig. 5a illustrates that all Ir(III) dopants possess a fitted energy level arrangement with respect to that of ν-DABNA and t-DABNA. Consequently, the sensitizers could suppress electron trapping in the EML. The concentration is optimized to 1 wt% to prevent undesired concentration quenching. As depicted in Table 5, as well as other literature precedents,[71–75] the incorporation of both ν-DABNA and t-DABNA has given substantial enhancements in efficiencies and reduction in FWHM. Moreover, the PLQYs of the blended thin film of ν-DABNA and t-DABNA with the same blending ratios of Ir(III) phosphors and the PPT host are provided in Table S2 of the ESI.† The high EQE$_{max}$ values of devices are in accordance with the results of the high PLQYs of blend-films. Notably, the EL performance of the f-Ir(tBpp)$_3$ sensitized device is generally better than those of f-Ir(dfpb)$_3$ and f-Ir(ptBp)$_3$ based devices. The deep blue hyper-OLED devices with f-Ir(tBpp)$_3$ have achieved remarkable EQE$_{max}$ values of 18.9% and 18.1% for terminal emitters ν-DABNA and t-DABNA, representing a substantial increase of EQE$_{max}$ with reference to that of the parent device (15.6%). Hence, these hyper-OLEDs also exhibited lower turn-on vol-

tages and higher maximum EQE and EQE at a brightness of 1000 cd m^{-2} in comparison to the pure MR-TADF devices recorded using ν-DABNA under identical device architecture.[69] Furthermore, the EL spectrum also exhibited a large reduction in FWHM from 58 nm for the parent device to 19 nm and 29 nm for terminal emitters ν-DABNA and t-DABNA, respectively.

Conclusion

In this work, we demonstrated the conceptual strategy of designing asymmetric carbene chelates for obtaining single Ir(III) carbene emitters through intra-chelate steric interactions. First, upon replacement of the phenyl substituent in carbene pro-chelate **C1** with a 4-t-butylphenyl substituent as shown in **C2**, the distribution of products changed from a mixed product ($i.e.$, both m-Ir(dfp)$_3$ and f-Ir(dfp)$_3$) to a single isomer, $i.e.$, f-Ir(dfpb)$_3$. This selectivity is probably attributed to the electron donating t-butyl group, which can increase the electron density at the Ir(III) metal center and, in turn, facilitate mer-to-fac isomerization under the applied synthetic conditions. On the other hand, this isomerization is not governed by the steric effect among three t-butyl groups, because this fac-orientation should exert a greater steric interaction than the mer-counterpart. Moreover, upon switching the carbene pro-chelates from **C1** and **C2** to **C3** and **C4**, both with dual N-aryl substituents, it is expected that both N-aryl groups can undergo competitive C–H activation and cyclometalation with the Ir(III) metal center affording four isomeric products as shown in our previous studies.[35–37] However, the $ortho$-substituted CF$_3$ group of **C3** and **C4** provides a second steric encumbrance, leading to the selective formation of only one product, namely f-Ir(tBpp)$_3$ and f-Ir(ptBp)$_3$, independent of the employed t-butylphenyl and phenyl appendages. Apparently, the imposed steric effect has forced this N-aryl group to rotate, which then reduced its chance to react with the Ir(III) metal center leading to direct cyclometalation. This selectivity is important for the possible mass production of relevant Ir(III) complexes if they are required in the future.

Moreover, all isolated fac-isomers exhibited high PLQYs and narrowed FWHMs. Among them, f-Ir(tBpp)$_3$ with aryl appendages showed narrow photoluminescence with FWHM = 60 nm and a high PLQY approaching 80%. The fabricated

OLED device using f-Ir(tBpp)$_3$ as an emitter delivered a maximum EQE of 15.6% with CIE(x,y) coordinates of (0.15, 0.16). Furthermore, these Ir(III) complexes can also serve as sensitizers to convey their energy to the MR-TADF terminal emitters ν-DABNA and t-DABNA to achieve a maximum EQE of 18.9% and 18.1% with CIE(x,y) coordinates of (0.12, 0.15) and (0.14, 0.10), respectively. The findings elaborated a unique strategy for the advancement of OLED technologies in displays and lighting luminaries. Further research in this direction holds great promise in unlocking energy-efficient and high-performance OLEDs.

Experimental section

General information and materials

Commercially available reagents were used without further purification. ^{1}H and ^{19}F NMR spectra were obtained with an NMR 400 MHz instrument (Bruker AVANCE III, BBO probe). Mass spectra were recorded on an Applied Biosystems 4800 Plus MALDI TOF/TOF analyzer using 2,5-dihydroxybenzoic acid as the matrix substance. TGA measurements were performed on a TA Instruments TGAQ50, at a heating rate of 10 °C min^{-1} under a nitrogen atmosphere.

Photophysical measurements

UV-Vis spectra were recorded with a UV-Visible NIR spectrophotometer system (HITACHI UH4150). The steady-state emission spectra were recorded with a spectrofluorometer (Fluormax-4) and the lifetime decay spectra were recorded with a photon-counting system (Edinburgh FLS980). All solution samples were degassed using at least three freeze–pump–thaw cycles. Photoluminescence quantum yields in solution were calculated using the standard sample which has a known quantum yield, while quantum yields in PMMA thin film were measured using an integrated sphere. Lifetimes were obtained using an Edinburgh FLS980 time-correlated single photon counting (TCSPC) system with an EPL-375 diode laser as the excitation source.

Electrochemistry

Cyclic voltammetry was measured with an electrochemical analyzer (CHI660) equipped with a three-electrode system (glassy carbon: working electrode, platinum wire: auxiliary electrode, and Ag/AgCl: reference electrode). Nitrogen-purged acetonitrile was used as a solvent and NBu$_4$PF$_6$ (0.1 M) was used as a supporting electrolyte. The potentials were referenced externally to the ferrocenium/ferrocene (Fc$^+$/Fc) couple.

Synthesis of *mer*-tris(1-methyl-3-phenyl-4,6-bis(trifluoromethyl)benzo[*d*]imidazol-2-ylidene-*C*,*C*$^{2'}$) iridium(III) (*m*-Ir (dfp)$_3$) and *fac*-tris(1-methyl-3-phenyl-4,6-bis(trifluoromethyl)benzo[*d*]imidazol-2-ylidene-*C*,*C*$^{2'}$)iridium(III) (*f*-Ir(dfp)$_3$). A mixture of **C1** (1.63 g, 3.3 mmol), IrCl$_3$(tht)$_3$ (0.56 g, 1.0 mmol), sodium acetate (1.64 g, 20 mmol), and degassed *t*-butylbenzene (50 mL) was heated at reflux overnight under N$_2$. After that, the solvent was removed under vacuum. The

residue was dissolved in CH$_2$Cl$_2$ (100 mL), washed with brine, dried over anhydrous Na$_2$SO$_4$ and then evaporated to dryness. The crude product was purified by column chromatography using petroleum ether/ethyl acetate (4/1, v/v) as an eluent (R_f for *m*-Ir(dfp)$_3$ = 0.5 and *f*-Ir(dfp)$_3$ = 0.3) to give pale yellow (*m*-Ir (dfp)$_3$) and colorless (*f*-Ir(dfp)$_3$) solids. Yield: 554 mg (45.3%, *m*-Ir(dfp)$_3$), 349 mg (28.6%, *f*-Ir(dfp)$_3$).

Selected spectroscopic data for m-Ir(dfp)$_3$. HRMS (ESI, ^{193}Ir): m/z 1223.1620 [M + H$^+$], calcd for C$_{48}$H$_{28}$F$_{18}$IrN$_6$: 1223.1717; ^{1}H NMR (400 MHz, acetone-d_6) δ 8.20 (s, 2H), 8.13 (s, 1H), 8.03 (s, 1H), 7.97 (s, 1H), 7.94 (s, 1H), 7.64 (d, J = 8.1 Hz, 1H), 7.61–7.53 (m, 2H), 6.95–6.79 (m, 5H), 6.62 (m, 4H), 3.72 (s, 3H), 3.70 (s, 3H), 3.57 (s, 3H); ^{19}F NMR (376 MHz, acetone-d_6) δ −53.00 (s, 3F), −53.07 (s, 3F), −53.21 (s, 3F), −61.71 (s, 3F), −61.73 (s, 3F), −61.74 (s, 3F). Anal. calcd for C$_{48}$H$_{27}$F$_{18}$IrN$_6$: C, 47.18; H, 2.23; N, 6.88. Found: C, 47.20; H, 2.58; N, 6.79.

Selected crystal data for m-Ir(dfp)$_3$. CCDC deposition number: 2110266.† C$_{48}$H$_{27}$F$_{18}$IrN$_6$; M = 1221.95; monoclinic; space group = P2$_1$/n; a = 9.3558(2) Å, b = 34.9470(8) Å, c = 14.2098(3) Å; β = 91.9000(10)°; V = 4643.44(18) Å^3; Z = 4; ρ_{calcd} = 1.748 g cm^{-3}; $F(000)$ = 2384.0, crystal size = 0.36 × 0.14 × 0.03 mm^3; λ(Mo-K$_\alpha$) = 0.71073 Å; T = 223 (2) K; μ = 2.990 mm^{-1}; 43 608 reflections collected, 9485 independent reflections (R_{int} = 0.0363), max. and min. transmission = 0.605 and 0.745, data/restraints/parameters = 9485/186/697, GOF = 1.021, final $R_1[I > 2\sigma(I)]$ = 0.0241 and wR_2(all data) = 0.0501.

Selected spectroscopic data for f-Ir(dfp)$_3$. HRMS (ESI, ^{193}Ir): m/z 1223.1585 [M + H$^+$], calcd for C$_{48}$H$_{28}$F$_{18}$IrN$_6$: 1223.1717; ^{1}H NMR (400 MHz, acetone-d_6) δ 8.15 (s, 3H), 8.00 (s, 3H), 7.64 (d, J = 8.0 Hz, 3H), 6.97–6.90 (m, 3H), 6.62–6.61 (m, 6H), 3.62 (s, 9H); ^{19}F NMR (376 MHz, acetone-d_6) δ −53.08 (s, 9F), −61.74 (s, 9F). Anal. calcd for C$_{48}$H$_{27}$F$_{18}$IrN$_6$: C, 47.18; H, 2.23; N, 6.88. Found: C, 47.25; H, 2.26; N, 6.91.

Synthesis of *fac*-tris(1-(4-(*t*-butyl)phenyl)-3-methyl-5,7-bis(trifluoromethyl)benzo[*d*]imidazolin-2-ylidene-*C*,*C*$^{2'}$)iridium(III) (*f*-Ir(dfpb)$_3$). This complex was prepared from chelate **C2** using a procedure in accordance with that reported for **C1** and IrCl$_3$(tht)$_3$, giving a single product of *f*-Ir(dfpb)$_3$ as white powder. Yield: 495 mg (35.6%).

Selected spectroscopic data for f-Ir(dfpb)$_3$. HRMS (ESI, ^{193}Ir): m/z 1391.3503 [M + H$^+$], calcd for C$_{60}$H$_{52}$F$_{18}$IrN$_6$: 1391.3595; ^{1}H NMR (400 MHz, acetone-d_6) δ 8.13 (s, 3H), 7.98 (s, 3H), 7.57 (d, J = 8.5 Hz, 3H), 6.99 (dd, J = 8.5, 2.3 Hz, 3H), 6.48 (d, J = 2.3 Hz, 3H), 3.57 (s, 9H), 1.01 (s, 27H); ^{19}F NMR (376 MHz, acetone-d_6) δ −52.74 (s, 9F), −61.71 (s, 9F). Anal. calcd for C$_{60}$H$_{51}$F$_{18}$IrN$_6$: C, 51.83; H, 3.70; N, 6.04. Found: C, 51.78; H, 3.69; N, 5.93.

Synthesis of *fac*-tris(1-(4-(*t*-butyl)phenyl)-3-phenyl-4,6-bis(trifluoromethyl)benzo[*d*]imidazolin-2-ylidene-*C*,*C*$^{2'}$)iridium(III) (*f*-Ir(tBpp)$_3$). A mixture of **C3** (394 mg, 0.64 mmol), IrCl$_3$(tht)$_3$ (110 mg, 0.2 mmol), sodium acetate (164 mg, 2 mmol), and degassed 1,2,4-trichlorobenzene (10 mL) was heated at reflux overnight under N$_2$. After that, the solvent was removed under vacuum. The residue was dissolved in CH$_2$Cl$_2$ (30 mL), washed with brine, dried over anhydrous Na$_2$SO$_4$ and, evaporated to dryness. The crude product was purified by column chromato-

2422 | *Inorg. Chem. Front.*, 2024, **11**, 2413–2426

This journal is © the Partner Organisations 2024

graphy using hexane/ethyl acetate (9/1, v/v) as an eluent to give a single product of *f*-**Ir(tBpp)₃** as white powder. Yield: 217 mg (69%).

Selected spectroscopic data for f-Ir(tBpp)₃. HRMS (ESI, [193]Ir): *m/z* 1577.3892 [M + H⁺], calcd for $C_{75}H_{58}F_{18}IrN_6$: 1577.4065; ^{1}H NMR (400 MHz, CDCl₃) δ 8.46 (s, 3H), 7.79 (d, *J* = 8.0 Hz, 3H), 7.71 (s, 3H), 7.62 (d, *J* = 8.4 Hz, 3H), 7.19 (td, *J* = 7.6, 1.2 Hz, 3H), 7.10 (dd, *J* = 8.4, 2.4 Hz, 3H), 6.59 (td, *J* = 8.0, 1.6 Hz, 3H), 6.49 (tt, *J* = 7.6, 1.2 Hz, 3H), 6.42 (d, *J* = 2.4 Hz, 3H), 6.08 (dt, *J* = 8.0, 1.6 Hz, 3H), 0.98 (s, 27H); ^{19}F NMR (376 MHz, CDCl₃) δ −56.25 (s, 9F), −61.03 (s, 9F). Anal. calcd for $C_{75}H_{57}F_{18}IrN_6$: C, 57.14; H, 3.64; N, 5.33. Found: C, 57.07; H, 3.60; N, 5.37.

Selected crystal data for f-Ir(tBpp)₃. CCDC deposition number: 2242122.† $C_{75}H_{57}F_{18}IrN_6$; *M* = 1576.46; trigonal; space group = $P\bar{3}$; *a* = 16.3890(5) Å, *b* = 16.3890(5) Å, *c* = 17.8634(5) Å; *γ* = 120°; *V* = 4155.3(3) Å³; *Z* = 2; ρ_{calcd} = 1.260 g cm⁻³; *F*(000) = 1576.0, crystal size = 0.29 × 0.14 × 0.04 mm³; λ(Cu–K$_\alpha$) = 1.54178 Å; *T* = 213 (2) K; *μ* = 3.811 mm⁻¹; 74 392 reflections collected, 5712 independent reflections (R_{int} = 0.0498), max. and min. transmission = 0.754 and 0.520, data/restraints/parameters = 5712/901/424, GOF = 1.068, final $R_1[I > 2\sigma(I)]$ = 0.0239 and wR_2(all data) = 0.0651.

Synthesis of *fac*-tris(1-phenyl-3-(4-(*t*-butyl)phenyl)-4,6-bis(tri-fluoromethyl)benzo[*d*]imidazolin-2-ylidene-*C*,*C*²′)iridium(III) (*f*-Ir(ptBp)₃). This complex was prepared from **C4** and IrCl₃(tht)₃ using a procedure in accordance with that reported for *f*-**Ir(tBpp)₃**, giving a single product of *f*-**Ir(ptBp)₃** as white powder. Yield: 150 mg (47%).

Selected spectroscopic data for f-Ir(ptBp)₃. HRMS (ESI, [193]Ir): *m/z* 1577.3932 [M + H⁺], calcd for $C_{75}H_{58}F_{18}IrN_6$: 1577.4065; ^{1}H NMR (400 MHz, CDCl₃) δ 8.57 (s, 3H), 7.80 (dd, *J* = 8.0, 1.2 Hz, 3H), 7.66 (s, 3H), 7.53 (dd, *J* = 8.4, 2.4 Hz, 3H), 7.36 (dd, *J* = 8.4, 2.4 Hz, 3H), 7.17 (td, *J* = 8.0, 1.6 Hz, 3H), 6.71 (td, *J* = 8.0, 1.2 Hz, 3H), 6.68 (dd, *J* = 8.0, 2.0 Hz, 3H), 6.54 (dd, *J* = 8.0, 2.0 Hz, 3H), 5.84 (dd, *J* = 8.0, 1.6 Hz, 3H), 0.84 (s, 27H).; ^{19}F NMR (376 MHz, CDCl₃) δ −56.09 (s, 9F), −61.18 (s, 9F). Anal. calcd for $C_{75}H_{57}F_{18}IrN_6$: C, 57.14; H, 3.64; N, 5.33. Found: C, 57.16; H, 3.66; N, 5.29.

Author contributions

J. Y., Y. P. and I. C. P.: investigation, experiments, data curation, writing – original draft preparation, and writing – review and editing. B. H., G. N. and S. M. Y.: experiments. W. Y. H., Y. C. and K. C. L.: funding acquisition, writing – review and editing, supervision, resources, funding acquisition, project administration, writing – original draft preparation, and writing – review and editing.

Conflicts of interest

The authors declare no competing financial interest.

References

1 M. L. Tang and Z. Bao, Halogenated Materials as Organic Semiconductors, *Chem. Mater.*, 2011, **23**, 446–455.

2 M. Stolar and T. Baumgartner, Organic n-type materials for charge transport and charge storage applications, *Phys. Chem. Chem. Phys.*, 2013, **15**, 9007–9024.

3 X. Zhou, P. L. Burn and B. J. Powell, Bond Fission and Non-Radiative Decay in Iridium(III) Complexes, *Inorg. Chem.*, 2016, **55**, 5266–5273.

4 R. Ragni, A. Punzi, F. Babudri and G. M. Farinola, Organic and Organometallic Fluorinated Materials for Electronics and Optoelectronics: A Survey on Recent Research, *Eur. J. Org. Chem.*, 2018, 3500–3519.

5 S. Dolui, D. Kumar, S. Banerjee and B. Ameduri, Well-Defined Fluorinated Copolymers: Current Status and Future Perspectives, *Acc. Mater. Res.*, 2021, **2**, 242–251.

6 F. Babudri, G. M. Farinola, F. Naso and R. Ragni, Fluorinated organic materials for electronic and opto-electronic applications: the role of the fluorine atom, *Chem. Commun.*, 2007, 1003–1022, DOI: **10.1039/B611336B**.

7 A. Y. Sosorev, M. K. Nuraliev, E. V. Feldman, D. R. Maslennikov, O. V. Borshchev, M. S. Skorotetcky, N. M. Surin, M. S. Kazantsev, S. A. Ponomarenko and D. Y. Paraschuk, Impact of terminal substituents on the electronic, vibrational and optical properties of thiophene–phenylene co-oligomers, *Phys. Chem. Chem. Phys.*, 2019, **21**, 11578–11588.

8 H.-B. Han, R.-Z. Cui, Y.-M. Jing, G.-Z. Lu, Y.-X. Zheng, L. Zhou, J.-L. Zuo and H. Zhang, Highly efficient orange-red electroluminescence of iridium complexes with good electron mobility, *J. Mater. Chem. C*, 2017, **5**, 8150–8159.

9 G.-Z. Lu, L. Liu, Z.-L. Tu, Y.-H. Zhou and Y. Zheng, Two green iridium(III) complexes containing the electron-trans-porting group of 4-phenyl-4H-1,2,4-triazole for highly efficient OLEDs, *J. Mater. Chem. C*, 2019, **7**, 2022–2028.

10 L. Zhang, Z.-P. Yan, Z.-L. Tu, Z.-G. Wu and Y.-X. Zheng, Green-emitting iridium(III) complexes containing pyridine sulfonic acid as ancillary ligands for efficient OLEDs with extremely low efficiency roll-off, *J. Mater. Chem. C*, 2019, **7**, 11606–11611.

11 Z. Chen, L. Wang, S. Su, X. Zheng, N. Zhu, C.-L. Ho, S. Chen and W.-Y. Wong, Cyclometalated Iridium(III) Carbene Phosphors for Highly Efficient Blue Organic Light-Emitting Diodes, *ACS Appl. Mater. Interfaces*, 2017, **9**, 40497–40502.

12 C. You, X.-Q. Wang, X. Zhou, Y. Yuan, L.-S. Liao, Y.-C. Liao, P.-T. Chou and Y. Chi, Homoleptic Ir(III) Phosphors with 2-Phenyl-1,2,4-triazol-3-ylidene Chelates for Efficient Blue Organic Light-Emitting Diodes, *ACS Appl. Mater. Interfaces*, 2021, **13**, 59023–59034.

13 R. Kumaresan, H.-Y. Park, A. Maheshwaran, H. Park, Y. Do, M. Song, J. Yoon, S. I. Ahn and S.-H. Jin, High Performance Solution-Processed Deep-Blue Phosphorescence Organic Light-Emitting Diodes with EQE Over 24% by Employing New Carbenic Ir(III) Complexes, *Adv. Opt. Mater.*, 2022, **10**, 2101686.

14 X.-K. Zheng, F.-Q. Zhao, M.-N. Yin, C. Qian, S.-H. Bi, P. Tao, Y.-Q. Miao, S.-J. Liu and Q. Zhao, New trifluoromethyl modified iridium(III) complex for high-efficiency sky-blue phosphorescent organic light-emitting diode, *Tetrahedron Lett.*, 2021, **75**, 153181.

15 J. Yan, Z.-H. Qu, D.-Y. Zhou, S.-M. Yiu, Y. Qin, X. Zhou, L.-S. Liao and Y. Chi, Bis-tridentate Ir(III) Phosphors and Blue Hyperphosphorescence with Suppressed Efficiency Roll-Off at High Brightness, *ACS Appl. Mater. Interfaces*, 2024, **16**, 3809–3818.

16 A. K. Pal, S. Krotkus, M. Fontani, C. F. R. Mackenzie, D. B. Cordes, A. M. Z. Slawin, I. D. W. Samuel and E. Zysman-Colman, High-Efficiency Deep-Blue-Emitting Organic Light-Emitting Diodes Based on Iridium(III) Carbene Complexes, *Adv. Mater.*, 2018, **30**, 1804231.

17 C. F. R. Mackenzie, L. Zhang, D. B. Cordes, A. M. Z. Slawin, I. D. W. Samuel and E. Zysman-Colman, Bulky Iridium NHC Complexes for Bright, Efficient Deep-Blue OLEDs, *Adv. Opt. Mater.*, 2023, **11**, 2201495.

18 G. Ni, J. Yan, Y. Wu, F. Zhou, P.-T. Chou and Y. Chi, Transition-metal phosphors with emission peak maximum on and beyond the visible spectral boundaries, *Inorg. Chem. Front.*, 2023, **10**, 1395–1401.

19 S. Lee and W.-S. Han, Cyclometalated Ir(iii) Complexes Towards Blue-Emissive Dopant for Organic Light-Emitting Diodes: Fundamentals of Photophysics and Designing Strategies, *Inorg. Chem. Front.*, 2020, **7**, 2396–2422.

20 A. Bonfiglio and M. Mauro, Phosphorescent Tris-Bidentate Ir[III] Complexes with N-Heterocyclic Carbene Scaffolds: Structural Diversity and Optical Properties, *Eur. J. Inorg. Chem.*, 2020, **2020**, 3427–3442.

21 T. Sajoto, P. I. Djurovich, A. B. Tamayo, J. Oxgaard, W. A. Goddard and M. E. Thompson, Temperature Dependence of Blue Phosphorescent Cyclometalated Ir(III) Complexes, *J. Am. Chem. Soc.*, 2009, **131**, 9813–9822.

22 K. Tsuchiya, S. Yagai, A. Kitamura, T. Karatsu, K. Endo, J. Mizukami, S. Akiyama and M. Yabe, Synthesis and Photophysical Properties of Substituted Tris(phenylbenzimidazolinato) Ir[III] Carbene Complexes as a Blue Phosphorescent Material, *Eur. J. Inorg. Chem.*, 2010, **2010**, 926–933.

23 J. Lee, H.-F. Chen, T. Batagoda, C. Coburn, P. I. Djurovich, M. E. Thompson and S. R. Forrest, Deep Blue Phosphorescent Organic Light-Emitting Diodes with Very High Brightness and Efficiency, *Nat. Mater.*, 2016, **15**, 92–98.

24 X. Yang, X. Zhou, Y.-X. Zhang, D. Li, C. Li, C. You, T.-C. Chou, S.-J. Su, P.-T. Chou and Y. Chi, Blue Phosphorescence and Hyperluminescence Generated from Imidazo[4,5-b]pyridin-2-ylidene Based Iridium(III) Phosphors, *Adv. Sci.*, 2022, **9**, 2201150.

25 A. Maheshwaran, V. G. Sree, H.-Y. Park, H. Kim, S. H. Han, J. Y. Lee and S.-H. Jin, High Efficiency Deep-Blue Phosphorescent Organic Light-Emitting Diodes with CIE x, y (<0.15) and Low Efficiency Roll-Off by Employing a High Triplet Energy Bipolar Host Material, *Adv. Funct. Mater.*, 2018, **28**, 1802945.

26 M. Idris, S. C. Kapper, A. C. Tadle, T. Batagoda, D. S. M. Ravinson, O. Abimbola, P. I. Djurovich, J. Kim, C. Coburn, S. R. Forrest and M. E. Thompson, Blue Emissive fac/mer-Iridium(III) NHC Carbene Complexes and their Application in OLEDs, *Adv. Opt. Mater.*, 2021, **9**, 2001994.

27 J. Yan, Q. Xue, H. Yang, S.-M. Yiu, Y.-X. Zhang, G. Xie and Y. Chi, Regioselective Syntheses of Imidazo[4,5-b]pyrazin-2-ylidene Based Chelates and Blue Emissive Iridium(III) Phosphors for Solution Processed OLEDs, *Inorg. Chem.*, 2022, **61**, 8797–8805.

28 J. Jin, Z. Zhu, J. Yan, X. Zhou, C. Cao, P.-T. Chou, Y.-X. Zhang, Z. Zheng, C.-S. Lee and Y. Chi, Iridium(III) Phosphors–Bearing Functional 9-Phenyl-7,9-dihydro-8H-purin-8-ylidene Chelates and Blue Hyperphosphorescent OLED Devices, *Adv. Photonics Res.*, 2022, **3**, 2100381.

29 Y. Qin, X. Yang, J. Jin, D. Li, X. Zhou, Z. Zheng, Y. Sun, W.-Y. Wong, Y. Chi and S.-J. Su, Facially Coordinated, Tris-bidentate Purin-8-ylidene Ir(III) Complexes for Blue Electrophosphorescence and Hyperluminescence, *Adv. Opt. Mater.*, 2022, **10**, 2201633.

30 Y. Chi and P.-T. Chou, Transition Metal Phosphors with Cyclometalating Ligands; Fundamental and Applications, *Chem. Soc. Rev.*, 2010, **39**, 638–655.

31 H. Yersin, A. F. Rausch, R. Czerwieniec, T. Hofbeck and T. Fischer, The Triplet State of Organo-Transition Metal Compounds. Triplet Harvesting and Singlet Harvesting for Efficient OLEDs, *Coord. Chem. Rev.*, 2011, **255**, 2622–2652.

32 T. Strassner, Phosphorescent Platinum(II) Complexes with C^C* Cyclometalated NHC Ligands, *Acc. Chem. Res.*, 2016, **49**, 2680–2689.

33 Z. Zheng, L. Wang, Y. Xin, Q. Wang, X. Hong, Y. Zhang, S.-M. Yiu, F. Zhou, J. Yan, D. Zhang, L. Duan and Y. Chi, Iridium(III) Carbene Phosphors with Fast Radiative Transitions for Blue Organic Light Emitting Diodes and Hyperphosphorescence, *Adv. Funct. Mater.*, 2024, **34**, 2311692.

34 J. Yan, C. Wu, K.-N. Tong, F. Zhou, Y. Chen, Y. Pan, G. Xie, Y. Chi, K.-C. Lau and G. Wei, Structural Engineering of Iridium(III) Phosphors with Imidazo[4,5-b]pyrazin-2-ylidene Cyclometalates for Efficient Blue Electroluminescence, *Small Methods*, 2024, **8**, 2301555.

2424 | *Inorg. Chem. Front.*, 2024, **11**, 2413–2426

This journal is © the Partner Organisations 2024

35 J. Yan, Y. Wu, I.-C. Peng, Y. Pan, S.-M. Yiu, K.-T. Wong, W.-Y. Hung, Y. Chi and K.-C. Lau, Peripheral engineering of Ir(III) emitters with imidazo[4,5-b]pyrazin-2-ylidene cyclometalates for blue organic light emitting diodes, *J. Mater. Chem. C*, 2023, **11**, 12270–12279.

36 J. Yan, D.-Y. Zhou, L.-S. Liao, M. Kuhn, X. Zhou, S.-M. Yiu and Y. Chi, Electroluminescence and hyperphosphorescence from stable blue Ir(III) carbene complexes with suppressed efficiency roll-off, *Nat. Commun.*, 2023, **14**, 6419.

37 J. Yan, Z.-Q. Feng, Y. Wu, D.-Y. Zhou, S.-M. Yiu, C.-Y. Chan, Y. Pan, K. C. Lau, L.-S. Liao and Y. Chi, Blue Electrophosphorescence from Iridium(III) Phosphors Bearing Asymmetric Di-N-Aryl 6-(trifluoromethyl)-2H-imidazo[4,5-b]pyridin-2-ylidene Chelates, *Adv. Mater.*, 2024, **36**, 2305273.

38 R. M. Roberts and P. J. Vogt, Ethyl N-phenylformimidate, *Org. Synth.*, 1955, **35**, 65–66.

39 E. B. Knott and R. A. Jeffreys, The structure of the solid reaction product of anilines and ethyl orthoformate, *J. Org. Chem.*, 1949, **14**, 879–885.

40 K. Hirano, A. T. Biju and F. Glorius, Copper-Catalyzed Synthesis of 2-Unsubstituted, N-Substituted Benzimidazoles, *J. Org. Chem.*, 2009, **74**, 9570–9572.

41 T. Lv, Z. Wang, J. You, J. Lan and G. Gao, Copper-Catalyzed Direct Aryl Quaternization of N-Substituted Imidazoles to Form Imidazolium Salts, *J. Org. Chem.*, 2013, **78**, 5723–5730.

42 Y.-C. Chiu, C.-H. Lin, J.-Y. Hung, Y. Chi, Y.-M. Cheng, K.-W. Wang, M.-W. Chung, G.-H. Lee and P.-T. Chou, Authentic-Blue Phosphorescent Iridium(III) Complexes Bearing Both Hydride and Benzyl Diphenylphosphine; Control of the Emission Efficiency by Ligand Coordination Geometry, *Inorg. Chem.*, 2009, **48**, 8164–8172.

43 J.-Y. Hung, C.-H. Lin, Y. Chi, M.-W. Chung, Y.-J. Chen, G.-H. Lee, P.-T. Chou, C.-C. Chen and C.-C. Wu, Phosphorescent Ir(III) Complexes Bearing Double Benzyldiphenylphosphine Cyclometalates; Strategic Synthesis, Fundamental and Integration for White OLED Fabrication, *J. Mater. Chem.*, 2010, **20**, 7682–7693.

44 J. G. Osiak, T. Setzer, P. G. Jones, C. Lennartz, A. Dreuw, W. Kowalsky and H.-H. Johannes, Twist it! The Acid-dependent Isomerization of Homoleptic Carbenic Iridium(III) Complexes, *Chem. Commun.*, 2017, **53**, 3295–3298.

45 N. Tamosiunaite, L. C. Logie, S. E. Neale, K. Singh, D. L. Davies and S. A. Macgregor, Experimental and Computational Studies on the Acetate-Assisted C–H Activation of N-Aryl Imidazolium Salts at Rhodium and Iridium: A Chloride Additive Changes the Selectivity of C–H Activation, *J. Org. Chem.*, 2022, **87**, 1445–1456.

46 A. Y. Gitlina, F. Fadaei-Tirani and K. Severin, The acid-mediated isomerization of iridium(III) complexes with cyclometalated NHC ligands: kinetic vs. thermodynamic control, *Dalton Trans.*, 2023, **52**, 2833–2837.

47 C. Wu, K. Shi, S. Li, J. Yan, Z.-Q. Feng, K.-N. Tong, S.-W. Zhang, Y. Zhang, D. Zhang, L.-S. Liao, Y. Chi, G. Wei and F. Kang, Design Strategies of Iridium(III) Complexes for Highly Efficient Saturated Blue Phosphorescent OLEDs with Improved Lifetime, *EnergyChem*, 2024, **6**, 100120.

48 C. Adamo and D. Jacquemin, The calculations of excited-state properties with Time-Dependent Density Functional Theory, *Chem. Soc. Rev.*, 2013, **42**, 845–856.

49 A. D. Laurent, C. Adamo and D. Jacquemin, Dye chemistry with time-dependent density functional theory, *Phys. Chem. Chem. Phys.*, 2014, **16**, 14334–14356.

50 R. L. Martin, Natural Transition Orbitals, *J. Chem. Phys.*, 2003, **118**, 4775–4777.

51 T. Lu and F. Chen, Multiwfn: A multifunctional wavefunction analyzer, *J. Comput. Chem.*, 2012, **33**, 580–592.

52 J. M. Younker and K. D. Dobbs, Correlating Experimental Photophysical Properties of Iridium(III) Complexes to Spin–Orbit Coupled TDDFT Predictions, *J. Phys. Chem. C*, 2013, **117**, 25714–25723.

53 P. Pander, A. V. Zaytsev, A. Sil, J. A. G. Williams, P.-H. Lanoe, V. N. Kozhevnikov and F. B. Dias, The role of dinuclearity in promoting thermally activated delayed fluorescence (TADF) in cyclometallated, N^C^N-coordinated platinum(II) complexes, *J. Mater. Chem. C*, 2021, **9**, 10276–10287.

54 P. Pander, L. Gomes Franca, F. B. Dias and V. N. Kozhevnikov, Electroluminescence of Tetradentate Pt (II) Complexes: O^N^N^O versus C^N^N^O Coordination, *Inorg. Chem.*, 2023, **62**, 5772–5779.

55 E. Jansson, P. Norman, B. Minaev and H. Ågren, Evaluation of low-scaling methods for calculation of phosphorescence parameters, *J. Chem. Phys.*, 2006, **124**, 114106.

56 E. Jansson, B. Minaev, S. Schrader and H. Ågren, Time-dependent density functional calculations of phosphorescence parameters for fac-tris(2-phenylpyridine) iridium, *Chem. Phys.*, 2007, **333**, 157–167.

57 K. Mori, T. P. M. Goumans, E. van Lenthe and F. Wang, Predicting phosphorescent lifetimes and zero-field splitting of organometallic complexes with time-dependent density functional theory including spin–orbit coupling, *Phys. Chem. Chem. Phys.*, 2014, **16**, 14523–14530.

58 M. A. Baldo, M. E. Thompson and S. R. Forrest, High-efficiency Fluorescent Organic Light-emitting Devices using a Phosphorescent Sensitizer, *Nature*, 2000, **403**, 750–753.

59 K. H. Lee and J. Y. Lee, Phosphor Sensitized Thermally Activated Delayed Fluorescence Organic Light-emitting Diodes with Ideal Deep Blue Device Performances, *J. Mater. Chem. C*, 2019, **7**, 8562–8568.

60 S. Nam, J. W. Kim, H. J. Bae, Y. M. Maruyama, D. Jeong, J. Kim, J. S. Kim, W.-J. Son, H. Jeong, J. Lee, S.-G. Ihn and H. Choi, Improved Efficiency and Lifetime of Deep-Blue Hyperfluorescent Organic Light-Emitting Diode using Pt(II) Complex as Phosphorescent Sensitizer, *Adv. Sci.*, 2021, **8**, 2100586.

61 A. Monkman, Why Do We Still Need a Stable Long Lifetime Deep Blue OLED Emitter?, *ACS Appl. Mater. Interfaces*, 2022, **14**, 20463–20467.

This journal is © the Partner Organisations 2024

Inorg. Chem. Front., 2024, **11**, 2413–2426 | **2425**

62 P. Zuo, Y.-K. Qu, Q. Zheng, L.-S. Liao and Z.-Q. Jiang, Sensitized organic light-emitting diodes: towards high efficiency and long lifetimes, *Mater. Chem. Front.*, 2023, **7**, 1760–1780.

63 D. Zhang, X. Song, A. J. Gillett, B. H. Drummond, S. T. E. Jones, G. Li, H. He, M. Cai, D. Credgington and L. Duan, Efficient and Stable Deep-Blue Fluorescent Organic Light-Emitting Diodes Employing a Sensitizer with Fast Triplet Upconversion, *Adv. Mater.*, 2020, **32**, 1908355.

64 C.-Y. Chan, M. Tanaka, Y.-T. Lee, Y.-W. Wong, H. Nakanotani, T. Hatakeyama and C. Adachi, Stable pure-blue hyperfluorescence organic light-emitting diodes with high-efficiency and narrow emission, *Nat. Photonics*, 2021, **15**, 203–207.

65 C. Duan, Y. Xin, Z. Wang, J. Zhang, C. Han and H. Xu, High-efficiency hyperfluorescent white light-emitting diodes based on high-concentration-doped TADF sensitizer matrices via spatial and energy gap effects, *Chem. Sci.*, 2022, **13**, 159–169.

66 K.-W. Lo, G. S. M. Tong, G. Cheng, K.-H. Low and C.-M. Che, Dinuclear Pt(II) Complexes with Strong Blue Phosphorescence for Operationally Stable Organic Light-Emitting Diodes with EQE up to 23% at 1000 cd m^{-2}, *Angew. Chem., Int. Ed.*, 2022, **61**, e202115515.

67 C. Wu, M. Wang, K.-N. Tong, M. Zhang, W. Li, Z. Xu, W.-L. Zhang, Y. Wu, C. Yang, H.-Y. Fu, S. S. Chen, M. Ng, M.-C. Tang and G. Wei, Blue Iridium(III) Phosphorescent OLEDs with High Brightness Over 10 000 cd m^{-2} and Ultralow Efficiency Roll-Off, *Adv. Opt. Mater.*, 2023, **11**, 2201998.

68 H. Liu, Y. Fu, J. Chen, B. Z. Tang and Z. Zhao, Energy-Efficient Stable Hyperfluorescence Organic Light-Emitting Diodes with Improved Color Purities and Ultrahigh Power Efficiencies Based on Low-Polar Sensitizing Systems, *Adv. Mater.*, 2023, **35**, 2212237.

69 J. Yan, S. F. Wang, C.-H. Hsu, E. H.-C. Shi, C.-C. Wu, P.-T. Chou, S.-M. Yiu, Y. Chi, C. You, I. C. Peng and W.-Y. Hung, Engineering of Cyano Functionalized Benzo[d]imidazol-2-ylidene Ir(III) Phosphors for Blue Organic Light-Emitting Diodes, *ACS Appl. Mater. Interfaces*, 2023, **15**, 21333–21343.

70 H. Shin, S. Lee, K.-H. Kim, C.-K. Moon, S.-J. Yoo, J.-H. Lee and J.-J. Kim, Blue Phosphorescent Organic Light-Emitting Diodes Using an Exciplex Forming Co-Host with the External Quantum Efficiency of Theoretical Limit, *Adv. Mater.*, 2014, **26**, 4730–4734.

71 Y. Kondo, K. Yoshiura, S. Kitera, H. Nishi, S. Oda, H. Gotoh, Y. Sasada, M. Yanai and T. Hatakeyama, Narrowband deep-blue organic light-emitting diode featuring an organoboron-based emitter, *Nat. Photonics*, 2019, **13**, 678–682.

72 S. H. Han, J. H. Jeong, J. W. Yoo and J. Y. Lee, Ideal Blue Thermally Activated Delayed Fluorescence Emission Assisted by a Thermally Activated Delayed Fluorescence Assistant Dopant Through a Fast Reverse Intersystem Crossing Mediated Cascade Energy Transfer Process, *J. Mater. Chem. C*, 2019, **7**, 3082–3089.

73 S. O. Jeon, K. H. Lee, J. S. Kim, S.-G. Ihn, Y. S. Chung, J. W. Kim, H. Lee, S. Kim, H. Choi and J. Y. Lee, High-efficiency, long-lifetime deep-blue organic light-emitting diodes, *Nat. Photonics*, 2021, **15**, 208–215.

74 W. J. Chung, K. H. Lee, M. Jung, K. M. Lee, H. C. Park, M.-S. Eum and J. Y. Lee, Over 30 000 h Device Lifetime in Deep Blue Organic Light-Emitting Diodes with y Color Coordinate of 0.086 and Current Efficiency of 37.0 cd A^{-1}, *Adv. Opt. Mater.*, 2021, **9**, 2100203.

75 Z.-L. Zhu, J. Yan, L.-W. Fu, C. Cao, J.-H. Tan, S.-F. Wang, Y. Chi and C.-S. Lee, Peripheral engineering of platinum(II) dicarbene pincer complexes for efficient blue hyperphosphorescent organic light-emitting diodes, *Mater. Chem. Front.*, 2023, **7**, 3398–3405.

2426 | *Inorg. Chem. Front.*, 2024, **11**, 2413–2426

This journal is © the Partner Organisations 2024